

Micro-second Timing of PSR B1821–24 with *Chandra*/HRC-S

Robert E. Rutledge¹, Derek W. Fox¹, S. R. Kulkarni¹, Bryan A. Jacoby¹, I. Cognard²,
D.Č.Čacker³, and Stephen S. Murray⁴

ABSTRACT

We perform absolute timing of PSR B1821–24 in M28, using a 50 ksec observation with *Chandra*/HRC-S. We have obtained the highest signal-to-noise X-ray pulsed lightcurve of this source to date, detecting two X-ray pulses, as well as significant non-pulsed emission – a persistent X-ray flux which comprises $15\pm3\%$ of the total X-ray flux of the pulsar. The Gaussian width of the sharp X-ray peak is $34\pm3\ \mu\text{s}$ in time, implying a size of the X-ray beam as it crosses the line of sight of $4.0\pm0.4\ \text{deg}$. We find evidence for a significant trailing component in both X-ray peaks of the pulse profile. Including three *RXTE*/PCA observations in our analysis, and tying the phases together using a radio ephemeris obtained at Nançay, we find the absolute phases in the X-ray wander with respect to this radio ephemeris by up to $60\ \mu\text{s}$, likely due to the variable dispersion measure, which changes the pulse arrival time in the radio band but not the X-ray band. The present analysis makes clear that study of pulsar timing noise properties in millisecond pulsars such as PSR B1821–24 – hitherto only studied at radio wavelengths, where variable dispersion measure requires a significant correction – can be studied at X-ray wavelengths, where the effect of variable dispersion measure is negligible. We also examine the known uncertainties in the absolute *Chandra*/HRC-S timing accuracy, which amount to $\pm12\ \mu\text{s}$. We limit the amount of linear drift in the relative timing accuracy of HRC-S to $<3\times10^{-10}\ \text{s s}^{-1}$.

Subject headings: stars: pulsars: general, stars: pulsars: individual (PSR B1821–24)

¹Division of Physics, Mathematics and Astronomy, California Institute of Technology, MS 130-33, Pasadena, CA 91125; rutledge@tapir.caltech.edu, srk@astro.caltech.edu, derekfox@astro.caltech.edu, baj@astro.caltech.edu

²Laboratoire de Physique et Chimie de l'Environnement - CNRS, UMR 6115 - F-45071 Orleans Cedex2 - France ; icognard@cnrs-orleans.fr

³Astronomy Department and Radio Astronomy Laboratory, University of California, Berkeley; Berkeley, CA 94720-3411; dbacker@astro.berkeley.edu

⁴Harvard-Smithsonian Center for Astrophysics, 60 Garden Street, Cambridge, MA 02138; ssm@head-cfa.harvard.edu

1. Introduction

PSR B1821–24 is an isolated, 3.05 ms pulsar, the first radio pulsar to be discovered in a globular cluster (Lyne et al. 1987). The object has been frequently timed (Lyne et al. 1987; Foster et al. 1988; Foster et al. 1991; Cognard et al. 1996; Backer & Sallmen 1997). Due to its low ecliptic latitude, it has also been used to study the distribution of the solar coronal plasma (see for example Cognard et al. 1996). PSR B1821–24 is the second brightest magnetospheric X-ray pulsar in the sky (Becker & Trümper 1999). The high X-ray luminosity and millisecond period makes this pulsar a preferred target for the study of pulsar emission, as well as an excellent target to tie the clocks of satellite-borne X-ray detectors to UTC (Rots et al. 1998; hereafter, R98).

The radio profile consists of three components, the height and width of which exhibit significant variation across the decimeter band (Backer & Sallmen 1997). In the 800 MHz band, the two most prominent peaks (RP1 and RP2, separated by 107.6 ± 1.4 degrees; Foster et al. 1991) have narrow widths (about $80 \mu\text{s}$). There is also a third broad component (RP3), which follows RP2 in phase (Backer & Sallmen 1997). The X-ray profile consists of two peaks (Saito et al. 1997). The ASCA clock was accurate to link the X-ray profile to the radio profile to no better than $200 \mu\text{s}$. Using RXTE, R98 demonstrated that XP1, the stronger component, arrived after RP1 by $62 \pm 13 \mu\text{s}$.

Recently, Becker et al. (2002; B02 hereafter) described *Chandra*/ACIS-S spectral observations of the field of M28 sensitive to an X-ray flux limit of $6 \times 10^{30} \text{ erg s}^{-1}$, finding 46 point sources. It was found that PSR B1821–24 had a phase average spectrum corresponding to $\alpha=1.2$ power-law with an equivalent Hydrogen column density $N_{\text{H}}=1.6 \times 10^{21} \text{ cm}^{-2}$, confirming earlier phase-average spectral analysis (Saito et al. 1997).

Here, we present a 50-ksec observation with the High Resolution Camera (HRC) aboard *Chandra* obtained with $15.625 \mu\text{s}$ temporal resolution (“S” mode). The principal goal of the observation was to tie the *Chandra* clock to UTC at the accuracy of $10 \mu\text{s}$, to describe the sources of uncertainty in the UTC time tie, and to confirm this tie with observations in the radio band. In addition, we present analysis of three *RXTE* observations. Finally, we took advantage of the imaging capability of the HRC and searched for pulsations in the 8 (of 12) brightest X-ray sources in the field.

The paper is organized as follows. In § 2 we describe the radio observations performed at Nançay, from which the pulsar ephemeris (uncorrected for a time-variable dispersion measure – DM) was derived. As the DM toward PSR B1821–24 varies significantly, we discuss the present knowledge of the DM as this affects our interpretation of the X-ray pulsar observations. In § 3 we describe the *Chandra* HRC-S observations and X-ray timing

analysis, for both PSR B1821–24 and for other X-ray sources detected in the field. In § 4, we describe RXTE/PCA timing analyses of PSR B1821–24, which confirm the relative timing of the pulsar. In § 5, we compare the *Chandra* and *RXTE* pulsed lightcurves, folded on the Nançay radio ephemeris. In § 6, we briefly discuss the implications of these observational results, and conclude.

2. Radio Observations at Nançay

The radio timing observations were conducted at the large decimetric radio telescope located near Nançay (France). The collecting area is $\sim 7000 \text{ m}^2$, equivalent to a 93 meter dish. The system temperature was typically $\sim 45 \text{ Jy}$ before the upgrade in 1999-2000, after which it was improved to 25 Jy . The maximum integration time of this transit telescope is 70 minutes. Timing observations of PSR B1821–24 are conducted 8 to 12 times a month at different radio frequencies.

At Nançay, the pulsar signal is de-dispersed by using a swept frequency oscillator (around 80MHz) in the receiver IF chain, at a frequency of $\sim 1410 \text{ MHz}$. The pulse spectra are produced by a digital autocorrelator with a frequency resolution between 6.25 and 25kHz, depending on the observing frequency. The station UT time scale is provided by a local Rubidium Frequency standard. The offset relative to the international UTC time scale was measured daily at 14hUT via the Observatory of Paris by a special-purpose receiver using TV signals until December 1995, with accuracy of $\pm 40 \text{ ns}$. After December 1995, a GPS common view system with the Observatory of Paris was adopted and an even better link was achieved. With the Nançay Timing System, the frequency of arrival is measured by cross-correlation of the integrated pulse spectrum with a pulse template. The template profiles are constructed by integration of individual pulse profiles detected during our observations. The frequency of arrival measured for a start time of the Nançay dedisperser is dual of the times of arrival measured by most other observatories. We will adopt the traditional term of Time Of Arrival (TOA) hereafter since the data analysis is ultimately based on pairs of times and frequencies of arrival.

The data have been analysed by our software AnTiOPE using the Jet Propulsion Laboratory Ephemeris DE405 for the Earth orbital motion and for the spatial reference frame and the conventional UTC time scale for time reference. The small corrections UT1-UTC for the Earth orientation have been applied. However, no corrections have been made for the time-variable DM in the direction of PSR B1821–24, which can affect the pulse TOA by as much as $\sim 50 \text{ } \mu\text{s}$ at 1410 MHz (see the following section). More details on the analysis can be found in Cognard et al. (1995).

For JPL ephemeris DE405, we performed an analysis using pulsar TOAs from 1996 through 2002. Proper motion was set to zero and position held constant. We used as time of origin MJD 51468.0 (Oct 17, 1999). Table 1 gives the rotational frequency and its first two derivatives, a time of origin (t_0) and the pulsar phase (ϕ) at t_0 , where $\phi = 0$ corresponds to the arrival of RP2, and has an average value of zero over the duration of the ephemeris. We refer to this ephemeris as the Nançay ephemeris.

2.1. Time-Dependent Dispersion Measure

The DM along the line of sight to PSR B1821–24 produces a finite time delay between photons with frequency ν_1 and ν_2 (Cognard et al. 1996):

$$\delta\text{DM} = \frac{\delta t_{\nu_1} - \delta t_{\nu_2}}{k} \frac{\nu_1^2 \nu_2^2}{\nu_2^2 - \nu_1^2}$$

which gives a linear relation between a change in the pulse TOA at 1410 MHz ($\delta T_{1410\text{ MHz}}$), compared with that at X-ray frequency (effectively, infinite frequency), and a change in the DM (δDM) of

$$\delta T_{1410\text{ MHz}} = 2.09 \times 10^{-3} \delta\text{DM sec}$$

Observations at radio wavelengths have found that the DM toward PSR B1821–24 varies significantly on a year’s timescale (Backer et al. 1993; Cognard & Lestrade 1997), with an time-average increase between 1989 Oct and 1996 Jan of $0.005 \text{ pc cm}^{-3} \text{ yr}^{-1}$, or $10 \mu\text{s yr}^{-1}$ at 1410 MHz; the increase in DM was not monotonic, but appears to be the result of a power spectrum of interstellar plasma turbulence (Cognard et al. 1996). In 1996 Jan, the DM was measured to be $119.847(2) \text{ pc cm}^{-3}$.

Radio observations from Nançay at 1280, 1410 and 1680 MHz, taken between Jan and Sept 2002, measured the DM. A mean value of $119.873(5) \text{ pc cm}^{-3}$ was observed, across a range spanning $119.865\text{--}119.883 \pm 0.010 \text{ pc cm}^{-3}$. This is comparable to the value expected by extrapolating the 1989-1996 time average increase.

Moreover, the increase in DM between 1996 Jan and the mean value for Jan-Sep 2002 result in a $\delta T_{1410\text{ MHz}} = 54 \pm 11 \mu\text{s}$.

3. *Chandra* Observations and Analysis

Observations were performed with the *Chandra*/HRC-S detector (Murray et al. 1998; Zombeck et al. 1995). The HRC-S has timing resolution of $15.625 \mu\text{s}$, a nominal energy response of 0.1-2 keV, and essentially no energy resolution. The observation began 2002 Nov 8 5:41 UT, integrating for 49148 sec and a total livetime of 49068 sec (see Table 2). Data were analysed using CIAO v2.3 and CALDB v2.18. The absolute astrometry of observation (from telescope pointing) was checked using the present knowledge of its accuracy⁵; no known astrometric problems were found, and the absolute pointing accuracy is $0.6''$, 1σ .

We identify PSR B1821–24 near its *Chandra* pointing position; a power-density spectrum of the X-ray source counts (Press et al. 1995) finds the pulsation with the appropriate period (≈ 327 Hz). We used PSR B1821–24 for absolute astrometry, adopting for its position the Nançay radio ephemeris position (see § 2).

We created an image using `wavdetect`, first binning the raw HRC image ($0.13175''$ per pixel) by a factor of 2 and searching for sources on scales of a factor of 1, 2 and 4 larger. The resulting reconstructed wavelet image is shown in Fig. 1. We detected 13 sources within $2.6'$ of the cluster center. For each source, the absolute positions, fixed relatively to the radio position of PSR B1821–24 and X-ray countrates are given in Table 3.

To obtain comparative background, we extracted counts from two circular regions $21''$ in radius, set off from the cluster center by $32''$ and $37''$, which did not include any identified point sources. In these, we found a total of 8583 background counts, which corresponds to a total of 9.7 ± 0.1 background counts in a $1''$ radius region.

B02 found an excess diffuse X-ray component associated with M28 which extends to the core radius, which they attribute to unresolved point sources. To examine the contribution to background from this diffuse component, as well as from the extended point-spread function of point sources inside the core, we examined the countrate in two $4.47''$ circles within the core radius, the boundaries of which are $>2''$ from any resolved point source. These regions had countrates of 11.5 ± 0.5 counts in a 1 arcsec radius region integrated over the livetime of the observation, an excess of 1.8 ± 0.5 counts over the more distant background regions, confirming the excess diffuse emission found by B02.

We assume a distance of 5.5 kpc to M28 (Harris 1996). Throughout, we apply an energy correction factor of $1.42 \times 10^{-11} \text{ erg cm}^{-2} \text{ s}^{-1}$ or $5.18 \times 10^{34} \text{ erg s}^{-1}$ (0.1-2.0 keV) per 1 HRC-S count/sec, which is the X-ray flux corrected for absorption, assuming $N_{\text{H}} = 1.6 \times 10^{21} \text{ cm}^{-2}$

⁵CIAO thread http://asc.harvard.edu/ciao/threads/arcsec_correction/index.html#calc_corr

and a power-law photon spectral slope of $\alpha = 1.2$, as observed for PSR B1821–24 (B02). Alternatively, 1 HRC-S count/sec is 4.23×10^{-11} erg cm $^{-2}$ s $^{-1}$ or 1.54×10^{35} erg s $^{-1}$ (0.5–8.0 keV), unabsorbed, approximately a factor of 3.0 higher than in the 0.1–2.0 keV band.

We process the raw event times in the following manner (see § 3.4 for the detailed discussion of time corrections and their uncertainties). The event times delivered (that is, which are given in the data files known as the event-1 and event-2 files) require two steps to place them in the JPL DE405 reference frame barycenter (TDB). First, they are corrected for *Chandra* command-control-data-management propagation time (see § 3.4) by adding:

$$\text{Corrected Event Time} = \text{Event Time} + 281 \mu\text{sec}$$

Second, we use **axbary** to convert the corrected event times to the JPL DE405 reference frame barycenter (TDB), using the level 1 *Chandra* ephemeris orbit file and the Nançay ephemeris position.

Counts from each source were extracted from within $\sim 2''$ circles around source positions. The time-average luminosity of PSR B1821–24, found from the average HRC-S background subtracted countrate, is $(4.0 \pm 0.2) \times 10^{32}$ erg s $^{-1}$ (0.1–2.0 keV), consistent with the time-average value found by B02 ($1.28 \pm 0.02 \times 10^{33}$ erg s $^{-1}$, 0.5–8.0 keV) after correcting for different passbands.

We performed a Fourier transform on the barycentered lightcurves, with the time resolution 15.625 μ s, 630262500 time bins, and a frequency resolution of 2.0308998×10^{-5} Hz using FFTW (Frigo & Johnson 1998). With the complex transform, we produced a Leahy-normalized power density spectrum (PDS; Leahy et al. 1983) of each source.

3.1. *Chandra*/HRC-S Timing Analysis of PSR B1821–24

Examination of the pulsar harmonics in the PDS show the pulsation is strongly detected up to the 16th harmonic. To obtain the best-fit frequency, we convolved the discrete Fourier transform window function with the PDS within ± 10 frequency bins of each harmonic for a trial frequency, and mapped the sum of the convolution as a function of trial frequency, with frequencies over-resolved by a factor of 32 (twice the number of harmonics), taking the peak of the curve to be the best-fit frequency 327.40562430(5) Hz, consistent with that determined from the radio ephemeris. The change in frequency over the course of our observation is small compared to our uncertainty.

After determining this frequency, we extracted data about the position of PSR B1821–24 within a $1''$ circle; this decreases our background counts by a factor of 4 over a $2''$ circle (from

$\sim 46 \pm 2$ to 11.5 ± 0.5). The enclosed number of counts decreased from 446 to 396 counts, indicating a loss of $\sim 15.4 \pm 0.5$ source counts (4%). Using the Nançay ephemeris (Table 1) to determine the relative pulsar phase at the time start time of the observation

$$\text{TSTART} = 50814.0 \text{ d(MJD)} + 153121000.174675 \text{ sec}$$

which we found to be $\phi(\text{TSTART}) = 0.0617(11)$ periods. We folded this data in time at the X-ray measured pulsar frequency, and corrected the phase to the Nançay radio ephemeris. This folded X-ray lightcurve is shown in Fig. 2 in differential and integral form.

Two X-ray peaks are evident in the pulsed lightcurve, a “sharp” peak near $\phi=0.64$ (XP1) and a “dull” peak near $\phi=0.21$ (XP2). XP1 is associated in phase with the radio component RP1; R98 found XP1 followed RP1 at 800 MHz by 20 ± 4 milli-periods. We refer to this X-ray peak XP1. XP2, however, has no obvious corresponding component in the radio band.

XP1 has a maximum countrate, averaged over $30.54 \mu\text{s}$, of $(67 \text{ counts}) / (0.01 \times 49.068 \text{ ksec}) = 135 \pm 16 \text{ HRC-S counts ksec}^{-1}$, corresponding to an intrinsic luminosity of $(7.0 \pm 0.7) \times 10^{33} \text{ erg s}^{-1}$ (0.1-2.0 keV). XP2 has an intrinsic peak luminosity of $(2.3 \pm 0.4) \times 10^{33} \text{ erg s}^{-1}$.

We examined counts outside of the main pulses to determine if they are consistent with the number expected from background. We summed all the counts, excluding those within a phase of ± 0.15 of XP1 and XP2, finding a total of 29 counts, where we expect 4.6 ± 0.2 counts due to background. This is a detection of excess counts with a probability of $< 3 \times 10^{-14}$ as being due to a fluctuation in the background countrate. Treating the excess counts as a constant intensity, the time-average countrate is $(29 - 4.6) / (0.40 \times 49.068 \text{ ksec}) = 1.2 \pm 0.2 \text{ HRC-S counts ksec}^{-1}$, which is $15 \pm 3\%$ of the time-average countrate of PSR B1821–24. The corresponding luminosity of the unpulsed component is $(6.2 \pm 1) \times 10^{31} \text{ erg cm}^{-2} \text{ s}^{-1}$ (0.1-2 keV).

3.2. Timing Analysis for Other Sources in the Field

Standard Fourier analysis searches (Press et al. 1995) are most appropriate for the sinusoidal or near-sinusoidal pulsations seen from isolated neutron star sources (Pavlov et al. 1999) and some X-ray binary pulsars (Wijnands & Van der Klis 1998). In searching for X-ray pulsations from fast radio pulsars, on the other hand, we anticipate a sharply-peaked pulse profile and a correspondingly rich harmonic spectrum (c.f. Sec. 3.2.2 of Ransom et al. 2002).

These expectations are borne out in the HRC-S dataset for PSR B1821–24 itself, which shows significant power out to the 23rd harmonic of its fundamental 3.05 ms period. The maximum single-harmonic power is found in the second harmonic, which has $\nu = 2\nu_s$ and $P_2 = 404$ in the Leahy et al. (1983) normalization, and the individual harmonic powers do not drop below the 99.9% confidence level until the 24th harmonic. In a blind search for pulsations in this dataset, the maximum-significance detection would come in a sum of the first 23 harmonics, which provide a total power of $P_{1-23} = 1894$ and a single-trial false-alarm probability of 1×10^{-367} .

Searches for a pulsar weaker than PSR B1821–24 should be more conservative in approach; reducing the observed harmonic powers of the pulsar by a factor of ten results in a most-significant detection for the sum of the first thirteen harmonics only, with the addition of further harmonics weakening the detection. We performed a pulse search of the strongest eight sources in the field, apart from PSR B1821–24, summing the first ten harmonics and covering the 0.001 Hz to 2 kHz frequency range for the fundamental. Even at the upper boundary of this frequency range, our tenth harmonic frequency is less than the 32 kHz Nyquist frequency of our observations.

We used the Z^2 search technique for photon event lists (Buccheri et al. 1983). At full frequency resolution, this results in roughly 10^8 independent trials and should allow us to be sensitive to summed powers of 95 or more, roughly 6.5% the strength of the signal for PSR B1821–24. We did not find any convincing candidate pulsations in this sample. In three cases, our maximum power exceeds the nominal threshold of 95, but only slightly less-significant triggers at unrelated frequencies are also apparent, which make the highest-power triggers not credible. We are not certain of the cause of this anomalous power, but note that the HRC detector is subject to deadtime effects, which will cause the photons from the pulsar PSR B1821–24 to impose non-Poisson patterns on the data of other sources in the field.

3.3. Comparison of Source Detections with the Results of B02

In Fig. 3a, we compare the HRC-S countrates with the ACIS-I countrates for all sources detected (in both detectors) within $160''$ of the center of M28. For the ACIS-I countrate, we summed the countrates in the 0.2-1.0 and 1.0-2.0 keV bands listed by B02. The different quantum efficiencies and background countrates make for different detection limits for the two detectors. For the sources which were detected in both observations, the relation between countrates in the two different detectors was approximately $I(\text{ACIS-I}) = (I(\text{HRC-S})/0.4 \text{ c ksec}^{-1}) \text{ c ksec}^{-1}$, with a systematic uncertainty of a factor of 2.

Two sources detected in the HRC observation were not detected by B02 (sources #3 and #12, using our numbering, Table 3). The brighter (#3), had an HRC countrate of 0.7 ± 0.1 c ksec $^{-1}$, which would produce an ACIS-I countrate of 1.1 c ksec $^{-1}$ (± 0.3 dex), well above the limit of < 0.12 c ksec $^{-1}$, if its spectrum were the same as the other detected sources. To account for the non-detection with ACIS-I, the photon spectral slope of source #3 would have to be $\alpha > 9$, which is far steeper than for any known X-ray source. We suggest that source #3 is variable. Source #12 was detected with HRC-S at 0.3 ± 0.1 c ksec $^{-1}$, which would produce an ACIS-I countrate of 0.8 (± 0.3 dex) c/ ksec $^{-1}$.

We did not detect 30 of the 41 sources detected by B02 in our 160'' image radius (undetected B02 sources in order of decreasing total countrate, using the numbering of B02: 28, 32, 30, 8, 14, 33, 21, 31, 16, 10, 20, 11, 6, 35, 39, 27, 24, 34, 7, 42, 9, 13, 40, 12, 18, 46, 43, 15, 44, 5). All of these would have had HRC-S countrates at or below the HRC-S detection limit, with the exception of B02's source #28, which was detected with ACIS-I at 3.2 ± 0.3 c ksec $^{-1}$, which would have produced 1.3 HRC-S c ksec $^{-1}$ (± 0.3 dex, assuming a similar spectrum as other detected sources), instead of < 0.3 c ksec $^{-1}$. Although this source was not found by *wavdetect*, we extracted counts from within a 1'' radius of the position found by B02, and found a background subtracted number of counts of 16 ± 5 , corresponding to 0.3 ± 0.1 c ksec $^{-1}$, indicating that the source has faded by a factor $> 4.3 \pm 2.2$.

Figure 3b shows HRC-S countrate vs. the softness ratio (0.2-1.0 keV/2.0-8.0 keV) for sources from B02 (B02sources 5, 6, 7, 9, 12, 15, 18, 34, 35, 39, 40, 42, 43, 44, and 46 were excluded because they have ACIS-I single-band countrates and/or softness ratios consistent with zero). The softness ratios of sources not detected by the HRC-S observation have large relative uncertainties, but as a group they are not spectrally harder than the sources we detected. Thus, most of the non-detections in the HRC-S seem to be due to the lower sensitivity of the HRC-S relative to the ACIS-I, most likely due to the higher background countrate in the HRC-S detector.

3.4. *Chandra* Timing Accuracy

The accuracy of the HRC event time tags (after correction for their location in telemetry - see Murray et al. 2002) is limited by: (1) digitization in the HRC time value; (2) the stability of the spacecraft clock relative to ephemeris time; and (3) knowledge of the absolute relation of the spacecraft time to UTC (that is, the command-control-data-management (CCDM) propagation time). The magnitude of each of these are tabulated in Table 4.

Event times for the HRC (HRC Team 1996) are generated by measuring the time of

the event since the beginning of a reference time (called the Science Header Frame, which occurs every eighth telemetry frame or $8 \times 0.25625 = 2.050$ sec). This relative event time is digitized to $15.625 \mu\text{s}$ due to the number of telemetry bits available (18 bits available to count the spacecraft interface unit clock that runs at 1.024 MHz or $0.9765625 \mu\text{s count}^{-1}$ so the HRC time tags are in units of 16 counts of this 1.024 MHz clock [= $15.626 \mu\text{s}$] to span the 2.050 sec interval). Thus the digitization uncertainty in HRC times is, on average, $5 \mu\text{s}$.

The spacecraft clock which governs the telemetry is based on the use of an ultra-stable oscillator (USO), running at a nominal frequency of 8.192 MHz, on board the observatory, with periodic time tagging of the spacecraft clock at the receiving ground stations of the Deep Space network (DSN). Typically, the Chandra Observatory will have a DSN contact for about 1 hour every 8 hours, during which real-time telemetry is received at the ground stations (as well as Solid State Recorder dumps). The real time data (usually 30 minutes or more) are time tagged with the antenna arrival time providing a series of correlations between the spacecraft clock counter (which has a nominal period of 0.25625 sec/count) and JPL ephemeris time. The Chandra Science Center Flight Operations Team (FOT) (Watson & Davis 2002) fit these correlations to a simple second order polynomial, and the residuals are analyzed to provide a measure of the stability of the clock. The typical rms residual measured from these data is $5 \mu\text{s}$ or less. The measurements show occasional excursions to $10 \mu\text{sec}$; monitoring of these correlations over the operational lifetime of the observatory has detected no larger anomalies in the spacecraft clock stability. There is an observed secular trend in the clock period (0.25625000905 sec/count to 0.25625001046 sec/count over a 1016 day interval), which is due to cumulative radiation dose to the electronics, and is fully compensated for through the correlation function. Thus, the uncertainty in the time-tag due to the stability of the spacecraft clock relative to ephemeris time is $\pm 5 \mu\text{s}$.

The knowledge of the absolute time for Chandra data comes from the time tagging of data at the receiving (ground) antenna, and a knowledge of all of the propagation time delays between the spacecraft and the antenna, and any delays at the ground station between the UTC clock and the time tagging. The FOT has determined the sum of all of the systematic delays – including the delay on the spacecraft – of $281.25 \mu\text{s}$ (Chandra Science Center Flight Operations Team 2002) which is the propagation time of the spacecraft clock through the various elements of the spacecraft command, control, and data management system (CCDM). These systematic delay times are believed to be accurate to $\pm 10 \mu\text{s}$. This uncertainty includes the resolution of the UTC clock at the antenna, errors in propagation delays due to orbit errors, errors in the CCDM propagation time, and errors in ground propagation times.

In the case of the Chandra science instrument time tagging, the CCDM propagation time is incorrectly applied to the event times during pipeline data processing and must be

removed from the distributed event times (that is, $T_{\text{correct}} = T_{\text{pipeline}} + 281 \mu\text{s}$, for both the Level 1 and Level 2 event files). However, this processing error is totally systematic and adds no additional uncertainty to the absolute time once it is corrected. Thus the overall uncertainty in absolute event time is estimated by assuming the three errors are uncorrelated and can be root square summed to yield $\sigma = \sqrt{5^2 + 10^2 + 5^2} = 12 \mu\text{s}$. Of these three sources of uncertainty, only the $10 \mu\text{s}$ CCDM propagation time can – in principle – be better characterized and eliminated as a source of uncertainty. Thus, future CCDM characterization may ultimately decrease the time-tag uncertainty to $\pm 7 \mu\text{s}$.

4. *RXTE*/PCA Observations and Analysis

We analysed all three observations performed with the *RXTE*/PCA as listed in Table 2, the first of which (Sept 1996) has previously been analysed (R98). During the Sept 1996 and Feb 1997 observations, all five PCU units were operating, while during the Nov 1999 observation, only three of the five PCU units were operating. We used FTOOLS v5.1A (release 16 Jan 2002). All data were obtained in Good Xenon mode, which has time resolution of 2^{-20}sec ($\sim 1 \mu\text{sec}$). We selected events detected in the first detector layer only with an approximate energy range of 2–24 keV, selecting all pulse height analyser (PHA) channels beginning at channel 0 (where the instrumental cut-off is 2 keV) and up to 24 keV, depending on the detector voltage settings.

We barycentered the events into the DE405 time system using **axbary** in the CIAO release used for the *Chandra* analysis; this applies the 16 μsec intrinsic delay of the PCA instrument, the *RXTE* fine clock corrections, and the addition of the **TIMEZERO** keyparameter. The absolute systematic uncertainty of the *RXTE*/PCA event times in TDB is estimated to be $\pm 5 \mu\text{s}$ after MJD 50567 (1997 Apr 29 UT), and $\pm 8 \mu\text{s}$ prior to MJD 50567⁶ (Table 4). This level of accuracy is established by calibration several times daily by the *RXTE* Mission Operations Center, ultimately limited by the accuracy of the ground clock used for this calibration at White Sands⁷. A detailed discussion of this timing calibration is given in R98. We used the Nançay ephemeris to calculate the phase of each event, and produced a folded pulsar lightcurve. In each, the background countrate is significant, such that the persistent countrate for the pulsar is well below the detection limit.

⁶<http://heasarc.gsfc.nasa.gov/docs/xte/time.news.html>

⁷<http://heasarc.gsfc.nasa.gov/docs/xte/abc/time.html>

5. Comparison of Observations in the Nançay Ephemeris

With the *Chandra* and *RXTE* folded lightcurves tied to the Nançay ephemeris, we compare the relative phases.

In Fig. 4, we show the three *RXTE*/PCA and *Chandra*/HRC-S lightcurves folded on the Nançay ephemeris. We fit Gaussians to XP1 and XP2, finding the phase relative to the Nançay ephemeris for XP1 (ϕ_1) and XP2 (ϕ_2) and the width (σ_1 and σ_2). For Obs. 1, due to the low signal-to-noise, we held σ_1 and σ_2 fixed at the average values of obs. 2 and 4, to obtain a best-fit in relative phase. We list these values in Table 7, with the *statistical* uncertainty in phase (not including the systematic uncertainties of $\pm 8 \mu\text{s}$ (obs. 1), $\pm 5 \mu\text{s}$ (obs. 2 and 3) and $\pm 14 \mu\text{s}$ (obs. 4)).

We calculated the shift in the phases of each component for each observation N, relative to the phases measured from obs. 2 ($(\phi_{1,\text{obs}2} - \phi_{1,\text{obs}N})/(327.4056 \text{ Hz})$ for XP1 and $(\phi_{2,\text{obs}2} - \phi_{2,\text{obs}N})/(327.4056 \text{ Hz})$ for XP2). The relative shifts in the phase of the two components in each observation are consistent, though typically with large uncertainties. However, we find significant phase shifts in obs. 3 and 4 relative to the radio ephemeris prediction and the observed phases of obs. 1 and 2.

To produce a tighter constraint on the relative phases of each observation, we calculated a cross-correlation function (Press et al. 1995) using a template pulse form, and taking obs. 2 as $\delta\phi = 0$. We used each of the pulsed lightcurves binned in phase with bin sizes of 0.01 phases ($30.54 \mu\text{s}$). We then calculated

$$CCF(j) = \sum_{i=1,n} I_i \times \left(\sum_{l=1,2} \frac{A_l}{\sigma_l} \exp - \frac{((i-j)/n - \phi_l)^2}{2\sigma_l^2} \right)$$

where i is the phase bin number, I_i is the number of counts in phase bin i , l is the pulse component, A_l is the relative normalization of the pulse component, σ_l is the Gaussian width, and ϕ_l is the centroid of the pulse component. The values of σ_l were taken as an average of all four observed values; ϕ_1 was taken as the best-fit value from obs. 2; $\phi_1 - \phi_2 = 162.5 \pm 0.7$ deg was found by taking a weighted average of all four values; and A_l are the best-fit values from the *Chandra* data (see Table 5). We fit a quadratic function to the peak of the CCF (taking only the highest five values), to determine the best-fit phase lag, which we give (as a time lag, the X-ray $\Delta T_{\text{obs}=2,N}$ – the relative time lag of obs. N from obs. 2) in Table 7, along with the statistical and systematic uncertainties.

5.1. Width of XP1, and the HRC-S Timing Precision

The HRC-S observation resolves XP1 with a Gaussian width $\sigma_1 = 0.0115(9)$ in phase, or $35 \mu\text{s}$ (Table 7), subtracting the digitization time in quadrature, this results in a width of $34 \pm 3 \mu\text{s}$.

We examined phases as a function of time since the observation start of all counts which arrived at phase ϕ_1 within a range of $\pm 2\sigma_1$ (we found 164 such counts). We found no obvious systematic deviations in the phase as a function of time, indicating that the width of this component is intrinsic to the pulsar, and not due to a systematic wandering of the absolute timing calibration. A fit of a constant phase using a χ^2 minimization technique (Bevington 1969), assuming an uncertainty in phase of 0.0115 (the width of XP1) found a best-fit constant phase to be an acceptable model ($\chi^2 = 127$, 163 degrees of freedom) for the phases of these counts.

Fitting a linear model for the mean phase as a function of time (best fit: $\chi^2 = 126$ for 162 dof) finds that the change in mean phase as a function of time is $< 6.3 \times 10^{-7}$ radians per second over the duration of the observation. This places a limit of $< 3 \times 10^{-10} \text{ s s}^{-1}$ (90% confidence) on a linear drift in the relative timing calibration of the HRC-S instrument.

5.2. Trailing X-ray Emission

Examination of Fig. 4 shows that the X-ray pulses are asymmetric, with greater emission trailing the main pulse than leading it. In XP1 and XP2, the number of counts in the phase range $[\phi_N + 2\sigma_N, \phi_N + 0.15]$ is 39 and 25, respectively; prior to the pulse, the number of counts in the phase range $[\phi_N - 0.15, \phi_N - 2\sigma_N]$ is 13 and 7, respectively. The probability of observing 39 counts when 13 are expected is 5×10^{-9} ; and of observing 25 counts when 7 are expected is 1×10^{-7} .

5.3. Radio and X-ray Pulsar Timing Noise

In Fig. 5, we show the history of the pulsar timing noise of PSR B1821–24 between 1996–2002, relative to the Nançay ephemeris. The radio $O - C$ values have the sign convention that, if the observed pulse arrives before the calculated value, then $O - C$ is negative. Deviations in the pulse arrival time of a magnitude as great as $\pm(50\text{--}60) \mu\text{s}$ have been observed due to a combination of pulsar timing noise and unmodelled propagation effects such as DM variations.

For comparison between the radio $O - C$ and the X-ray ΔT , we estimated the radio $O - C$ value, by taking an average of the five nearest (in time) radio observations, and using the scatter of the value as the uncertainty (listed in Table 7). For comparison with the X-ray, we then set all values of the radio $O - C$ taken at the time of the four X-ray observations to be relative to that measured for obs. 2. We show the derived O-C values in Fig. 5. While the X-ray and radio O-C values match in observations #1 and 2, they are discrepant in observations #3 and 4.

In Fig. 6, we plot the pulsar time delay in the radio band relative to that observed in obs. 2 as a function of the time delay in the X-ray band relative to that observed in obs. 2; thus, the value corresponding to obs. 2 lies at the origin. The two observations (#3 and 4) are consistent with an absolute offset of the X-ray time delay from the radio time delay, found by a χ^2 best-fit assuming an X-ray/radio delay slope of 1 and neglecting the uncertainty in the radio phase:

$$\text{X-ray } \Delta T = \text{Radio}(O - C) - 51 \pm 7 \mu\text{sec}$$

A direct offset in the TOA phase of this magnitude can be explained by an increase in DM between observation 2 and 3 of 0.023 pc cm^{-3} , which is consistent with observations (see § 2.1).

The uncertainty in the position and proper motion of the pulsar will not affect the relative X-ray/radio phase offset, such as that we see in Fig. 6. An incorrect geometric assumption which results in a deviation in the radio pulse phase relative to the baseline ephemeris will also result in a deviation in the X-ray pulse phase measured at the same time, since a deviation in geometry affects only light travel time, affecting the X-ray and radio bands equally, which is not what we observe.

5.3.1. The Absolute Phase of X-ray Component 1

In the Nançay ephemeris, the phase $\phi = 0$ corresponds to an average phase over the duration of the ephemeris of zero for RP2. Assuming that $\phi_{\text{radio},2} - \phi_{\text{radio},1} = 0.299(4)$ (Foster et al. 1991), and taking the $\phi_{\text{X-ray},1(\text{R98})} - \phi_{\text{radio},1} = 0.020(4)$ from R98, we can find the difference between the presently measured phase of XP1 and that from the phasing of R98:

$$\phi_{\text{X-ray},1} - \phi_{\text{X-ray},1(\text{R98})} = \phi_{\text{X-ray},1} - \left[1 + \frac{\text{Radio}(O - C)}{3.054\text{ms}} - 0.299(4) \right] - 0.020(4) \quad (1)$$

Taking values from Table 7, we find that for observations 1-4, this difference amounts to $-180 \pm 20 \mu\text{s}$, $-180 \pm 20 \mu\text{s}$, $-230 \pm 20 \mu\text{s}$, and $-250 \pm 20 \mu\text{s}$, respectively. Thus, all four measured values of the X-ray phases for XP1 in the present work are in disagreement with that found by R98, including obs. 1 (the same data as analysed by R98).

It is difficult to see how the present measurements can be resolved with that of R98. The relative phase of XP1 is similar in all three RXTE observations (within $60 \mu\text{s}$) to that of the *Chandra* phase, within the Nançay ephemeris – a smaller variation than the $\sim 200 \mu\text{s}$ discrepancy. As we find similar phases in both the *Chandra*/HRC-S observation and the three RXTE/PCA observations, it does not appear to be due to a satellite calibration issue. The discrepancy may be due in part to the differing radio ephemeris of Nançay with that used by R98 (found using Green Bank and Jodrell Bank Telescopes and a different observational techniques, in a different radio passband). DM corrections were applied to the R98 ephemeris, although not to the present ephemeris; however, the variable DM can amount to at most $\sim 50 \mu\text{s}$ delay, which is smaller than the $-180 \mu\text{s}$ to $-250 \mu\text{s}$ difference we see here.

This issue can be examined more closely with an analysis which ties the Nançay ephemeris to observations at Green Bank, which is underway presently (Backer & Cognard, in progress).

6. Discussion and Conclusions

We have performed fast timing of PSR B1821–24 with *Chandra*/HRC-S, resolving the sharpest X-ray peak XP1 with a width $34 \pm 3 \mu\text{s}$. This also serves as a limit on a random timing calibration uncertainty variation over this 50 ksec observation. In addition, we place a limit of $< 3 \times 10^{-10} \text{ s s}^{-1}$ (90% confidence) on a linear-drift in the relative timing calibration of the HRC-S. Moreover, the Gaussian width of this component limits the width of the X-ray pulse beam as it passes across the line of sight to be 4.0 ± 0.4 degrees.

We detect for the first time persistent X-ray emission in PSR B1821–24, at a level of $15 \pm 3\%$ of the time-average X-ray flux, assuming identical spectra for the pulsed and non-pulsed emission. We also find trailing X-ray emission, significantly in excess of the emission leading both pulse components.

The absolute tie of the HRC-S instrument to TDB/UTC time standard compared with the known $\pm 5 \mu\text{s}$ capability of *RXTE* is confirmed with the precision limited by the alignment of the XP1 relative to the Nançay ephemeris of the HRC-S and three *RXTE*/PCA datasets. We observe that the four pulse lightcurves are significantly mis-aligned, offset by as much as $67 \mu\text{s}$. This mis-alignment appears to be due to the time-variable DM in the

direction of PSR B1821–24 over the 1996-2002 period, during which the *RXTE* and *Chandra* observations were made. The known time-dependent DM, measured elsewhere, results in a change in the TOA of the radio pulse – but not in the X-ray pulse – of the order of that observed.

A correction to the radio pulse TOA can be applied to the Nançay data, using DM measurements obtained at Nançay in the radio band taken from 1996-2002. This analysis is under way (Backer and Cognard, in progress). Once this correction is applied, the radio pulsed lightcurve data can be aligned absolutely in phase with the X-ray pulsed lightcurve, which can confirm *in situ* the *Chandra*/HRC-S absolute timing capability to the accuracy of the known uncertainties in the RXTE timing ($\pm 5 \mu\text{s}$) and the *Chandra*/HRC-S timing ($\pm 12 \mu\text{s}$).

Pulsar timing noise has yet to be measured in the X-ray band. The present observations demonstrate that the technical capability exists to do so for PSR B1821–24 in the presently operating X-ray observatories *RXTE* and *Chandra*. Repeated X-ray timing observations of PSR B1821–24 would produce a pulse-ephemeris independent of the effects of a time-varying DM, without having to measure the DM for each observation as required for this and other millisecond pulsars (such as PSR 1551+32, Foster et al. 1990; PSR 1821+05, Frail et al. 1991; PSR 1557-50, Deshpande et al. 1992; PSR 1855+09, PSR 1937+21, Backer et al. 1993; Cognard et al. 1995). Thus, the X-ray band provides the capability of measuring pulsar timing noise without a time-variable DM correction. Such observations would provide confirmation of the attribution of pulsar timing noise to spin-down processes, rather than for example, to processes associated with magnetospheric emission.

This work was supported by the *Chandra* Guest Observer program. The Nançay Radio Observatory is part of the Observatoire de Paris, associated to the French Centre National de la Recherche Scientifique (CNRS). The Nançay Observatory also gratefully acknowledges the financial support of the Conseil Regional of the Region Centre in France.

References

- Backer, D. C., Hama, S., van Hook, S., & Foster, R. S., 1993, ApJ 404, 636
- Backer, D. C. & Sallmen, S. T., 1997, AJ 114, 1539
- Becker, W., Swartz, D., Pavlov, G., Elsner, R., Grindlay, J., Mignani, R., Tennant, A.,
Backer, D., & Weisskopf, M., 2002, A&A, astro-ph/0211468
- Becker, W. & Trümper, J., 1999, A&A 341, 803

- Bevington, P. R., 1969, *Data Reduction and Error Analysis for the Physical Sciences*, McGraw-Hill
- Buccheri, R., Bennett, K., Bignami, G. F., Bloemen, J. B. G. M., Boriakoff, V., Caraveo, P. A., Hermsen, W., Kanbach, G., Manchester, R. N., Masnou, J. L., Mayer-Hasselwander, H. A., Ozel, M. E., Paul, J. A., Sacco, B., Scarsi, L., & Strong, A. W., 1983, *A&A* 128, 245
- Chandra Science Center Flight Operations Team, 2002, *Absolute Timing Accuracy*, Technical report, Center for Astrophysics
- Cognard, I., Bourgois, G., Lestrade, J. ., Biraud, F., Aubry, D., Darchy, B., & Drouhin, J. ., 1996, *A&A* 311, 179
- Cognard, I., Bourgois, G., Lestrade, J.-F., Biraud, F., Aubry, D., Darchy, B., & Drouhin, J.-P., 1995, *A&A* 296, 169
- Cognard, I. & Lestrade, J.-F., 1997, *A&A* 323, 211
- Deshpande, A. A., McCulloch, P. M., Radhakrishnan, V., & Anantharamaiah, K. R., 1992, *MNRAS* 258, 19P
- Foster, R. S., Backer, D. C., Taylor, J. H., & Goss, W. M., 1988, *ApJ* 326, L13
- Foster, R. S., Backer, D. C., & Wolszczan, A., 1990, *ApJ* 356, 243
- Foster, R. S., Fairhead, L., & Backer, D. C., 1991, *ApJ* 378, 687
- Frail, D. A., Cordes, J. M., Hankins, T. H., & Weisberg, J. M., 1991, *ApJ* 382, 168
- Frigo, M. & Johnson, S. G., 1998, in *ICASSP, Conference Proceedings, Vol. 3*, pp 1381–1384
- Harris, W. E., 1996, *AJ* 112, 1487
- HRC Team, 1996, *The High Resolution Camera (HRC) Description*, <http://www.harvard.edu/HRC/overview/overview.html>
- Leahy, D. A., Darbro, W., Elsner, R. F., Weisskopf, M. C., Kahn, S., Sutherland, P. G., & Grindlay, J. E., 1983, *ApJ* 266, 160
- Lyne, A. G., Brinklow, A., Middleditch, J., Kulkarni, S. R., & Backer, D. C., 1987, *Nature* 328, 399
- Murray, S. S., Chappell, J. H., Kenter, A. T., Kraft, R. P., Meehan, G. R., & Zombeck, M. V., 1998, in *Proc. SPIE Vol. 3356, p. 974-984, Space Telescopes and Instruments V, Pierre Y. Bely; James B. Breckinridge; Eds.*, Vol. 3356, p. 974
- Murray, S. S., Ransom, S. M., Juda, M., Hwang, U., & Holt, S. S., 2002, *ApJ* 566, 1039
- Pavlov, G. G., Zavlin, V. E., & Trümper, J., 1999, *ApJ* 511, L45
- Press, W., Flannery, B., Teukolsky, S., & Vetterling, W., 1995, *Numerical Recipes in C*, Cambridge University Press
- Ransom, S. M., Eikenberry, S. S., & Middleditch, J., 2002, *AJ* 124, 1788
- Rots, A. H., Jahoda, K., Macomb, D. J., Kawai, N., Saito, Y., Kaspi, V. M., Lyne, A. G., Manchester, R. N., Backer, D. C., Somer, A. L., Marsden, D., & Rothschild, R. E., 1998, *ApJ* 501, 749

- Saito, Y., Kawai, N., Kamae, T., Shibata, S., Dotani, T., & Kulkarni, S. R., 1997, *ApJ* 477, L37
- Watson, M. & Davis, W., 2002, *Chandra Clock Correlation Summary*, Technical report, Center for Astrophysics
- Wijnands, R. & Van der Klis, M., 1998, *Nature* 394, 344
- Zombeck, M. V., Chappell, J. H., Kenter, A. T., Moore, R. W., Murray, S. S., Fraser, G. W., & Serio, S., 1995, in *Proc. SPIE Vol. 2518, p. 96-106, EUV, X-Ray, and Gamma-Ray Instrumentation for Astronomy VI*, Oswald H. Siegmund; John V. Vallerga; Eds., Vol. 2518, p. 96

Fig. 1.— Wavelet reconstructed image of *Chandra*/HRC-S observation centered on M28 (cross), showing the locations of X-ray sources detected within the half-mass radius (outer circle, $93.6''$ radius). The small circle marks the $14.4''$ core radius. The cross marks the optical cluster center (Harris 1996). The $11.27'$ tidal-radius is much larger than the image. Sources 8, 9, and 10 are not included in this figure, as they are well outside the half-mass radius (their positions are listed in Table 3).

Fig. 2.— The *Chandra* HRC-S phase-binned lightcurve of PSR B1821–24, folded on the pulsar period (~ 3.05 msec), and aligned to the absolute phase of Nançay ephemeris. There are 9.7 ± 0.1 background counts in this lightcurve (total). The counts detected outside the main pulse are significantly above background, indicating pulsar bridge emission at the level of $15 \pm 3\%$ of the total X-ray flux (0.1–2.0 keV)

Fig. 3.— **Panel (a):** The HRC-S countrate vs. ACIS-I countrate (0.2–2 keV; from B02), for sources detected within $160''$ of the center of M28. Down to a countrate limit of 2 ACIS-I c ksec $^{-1}$, all sources are detected in the HRC-S with the exception of B02 source #28 at 3.1 ACIS-I c ksec $^{-1}$, but < 0.3 HRC-S c ksec $^{-1}$. Down to a countrate limit of 0.4 HRC-S c ksec $^{-1}$, all sources are detected with ACIS-I, with the exception of our source #3 at 0.7 HRC-S c ksec $^{-1}$, but < 0.12 ACIS-I c ksec $^{-1}$. (N.B. the ACIS-I countrate upper-limits are estimated from the < 0.2 c ksec $^{-1}$ upper limit for the full 0.2–8 keV energy range, decreased by $\sim 60\%$, assuming a $\alpha=1.4$ photon power-law spectrum). **Panel (b):** The HRC-S countrate vs. the ACIS-I softness ratio (0.2–1.0 keV/2.0–8.0 keV). The non-detections in the HRC-S of sources detected with the ACIS-I do not appear to be correlated with spectrum.

Fig. 4.— The pulsar lightcurves observed (from top to bottom) with RXTE/PCA (1996 Sept, 1997 Feb, and 1999 Nov), and *Chandra*/HRC-S (2002 Nov), folded on the Nançay ephemeris. The component number 1 and 4 (XP1 and XP2) are labeled in the second panel from the top. Note that XP1, near $\phi=0.65$, do not align in the Nançay ephemeris, likely due to the absence of DM-variability corrections in the Nançay ephemeris.

Fig. 5.— The Observed minus Calculated (O-C) zero-phase arrival time (of RP2) of PSR B1821–24 using the Nançay ephemeris, as a function of time (small dots). The top axis is marked in UT years, the bottom axis in MJD. Deviations as great as $67 \mu\text{s}$ have been observed. The $O - C$ value for the Nançay radio observations at the time of the X-ray observations (open squares) and for the four X-ray observations (crosses). The radio data are given in absolute phase (uncorrected for changes in DM), whereas the X-ray points are taken relative to the phase of Observation #2 (MJD 50489). The X-ray points for observations #3 and #4 are discrepant with the O-C values found from radio data. The magnitude and sign of the discrepancy is consistent with that expected from the observed change in DM between 1996 and 2002.

Fig. 6.— The X-ray pulse time delay, as a function of radio pulse time delay, both taken relative to obs. 2 (which therefore lies at the origin). The uncertainty in the values for obs. 2 are shown on that data point, although this uncertainty is also reflected in the uncertainties of the other points. The values for obs. 3 and 4 lie clearly away from a relationship in which the pulsar timing noise is of equal magnitude in both the radio and X-ray bands. This discrepancy can be explained as due the variable DM (see § 2.1).

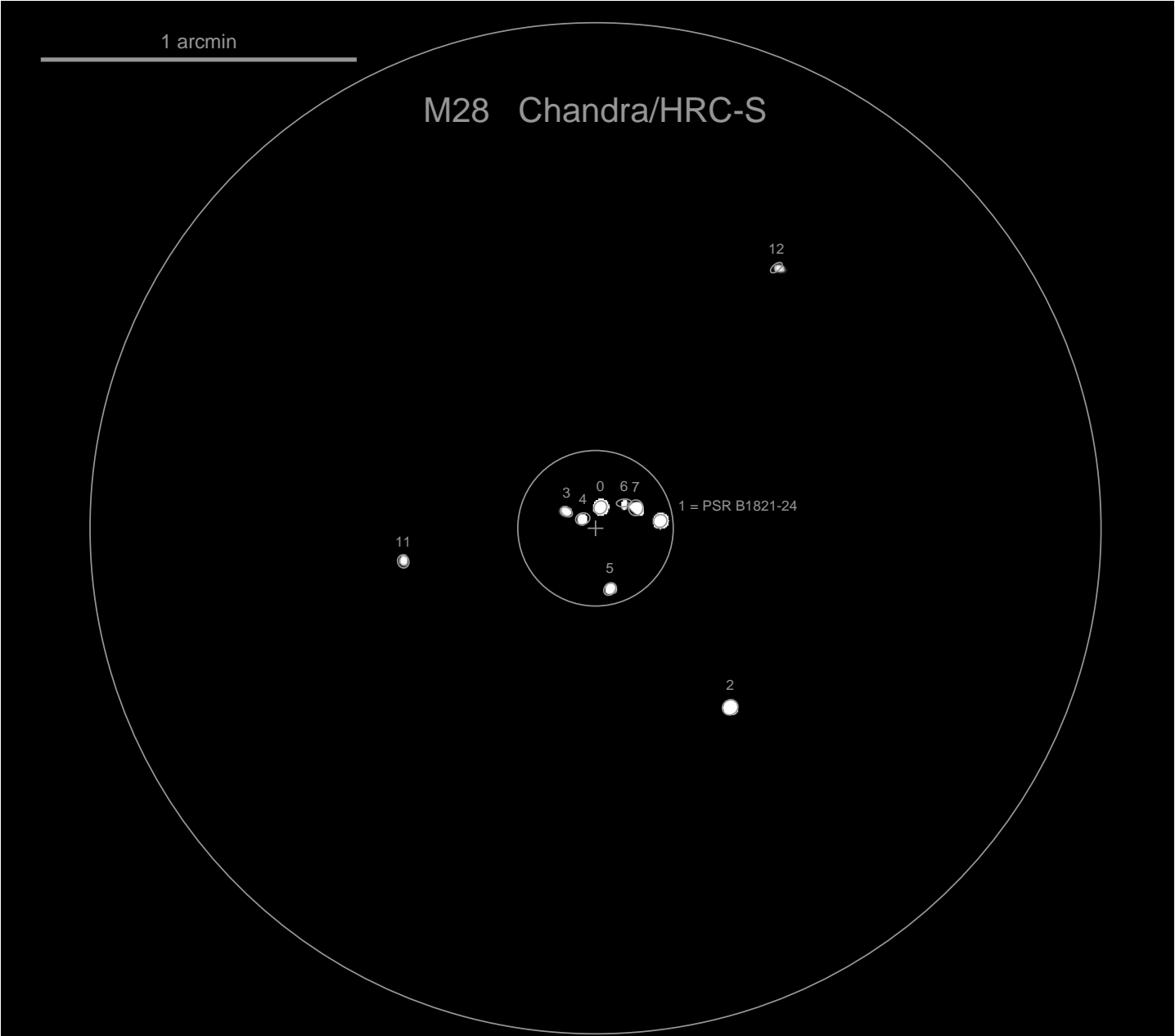


Figure 1

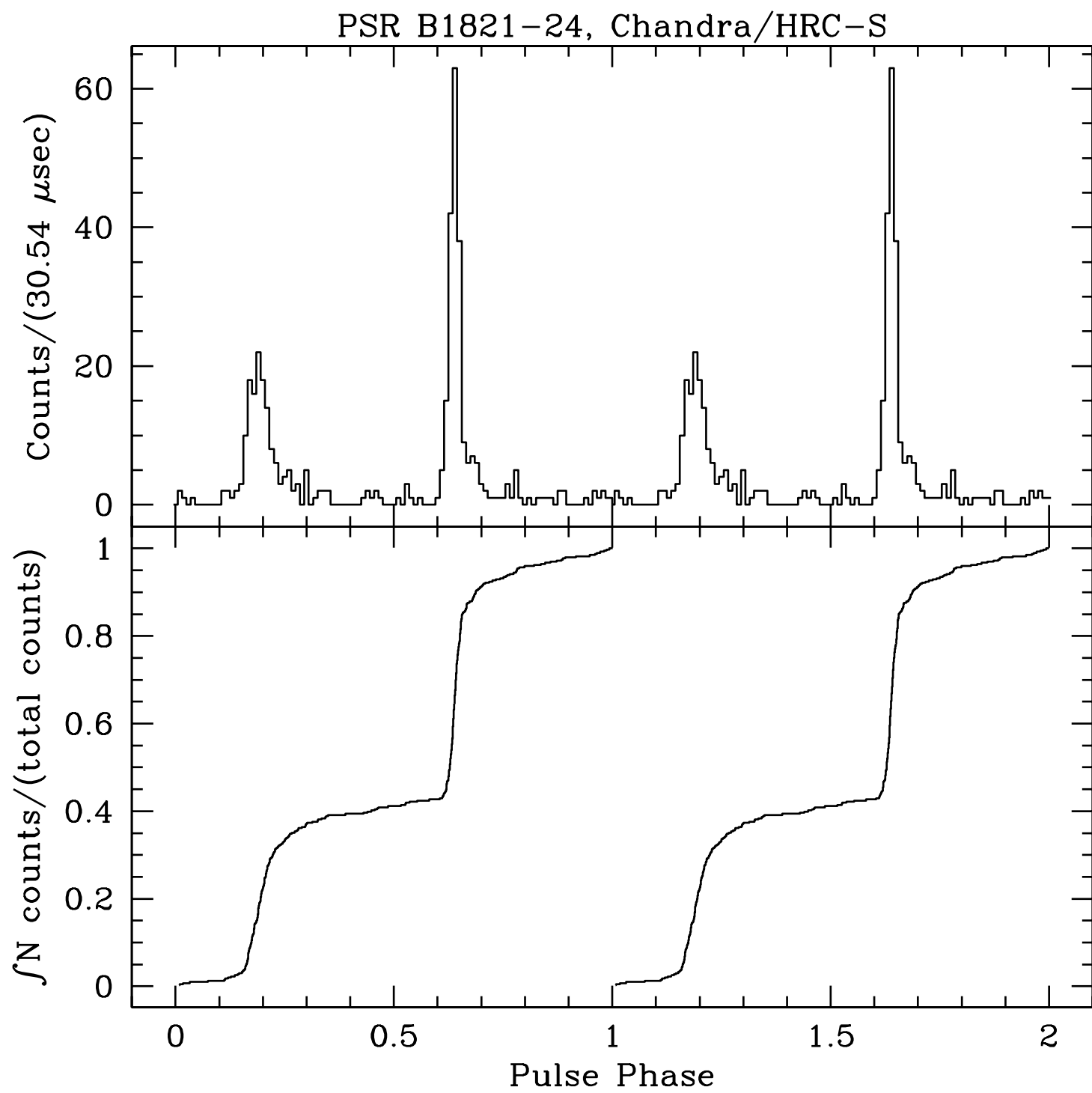


Figure 2

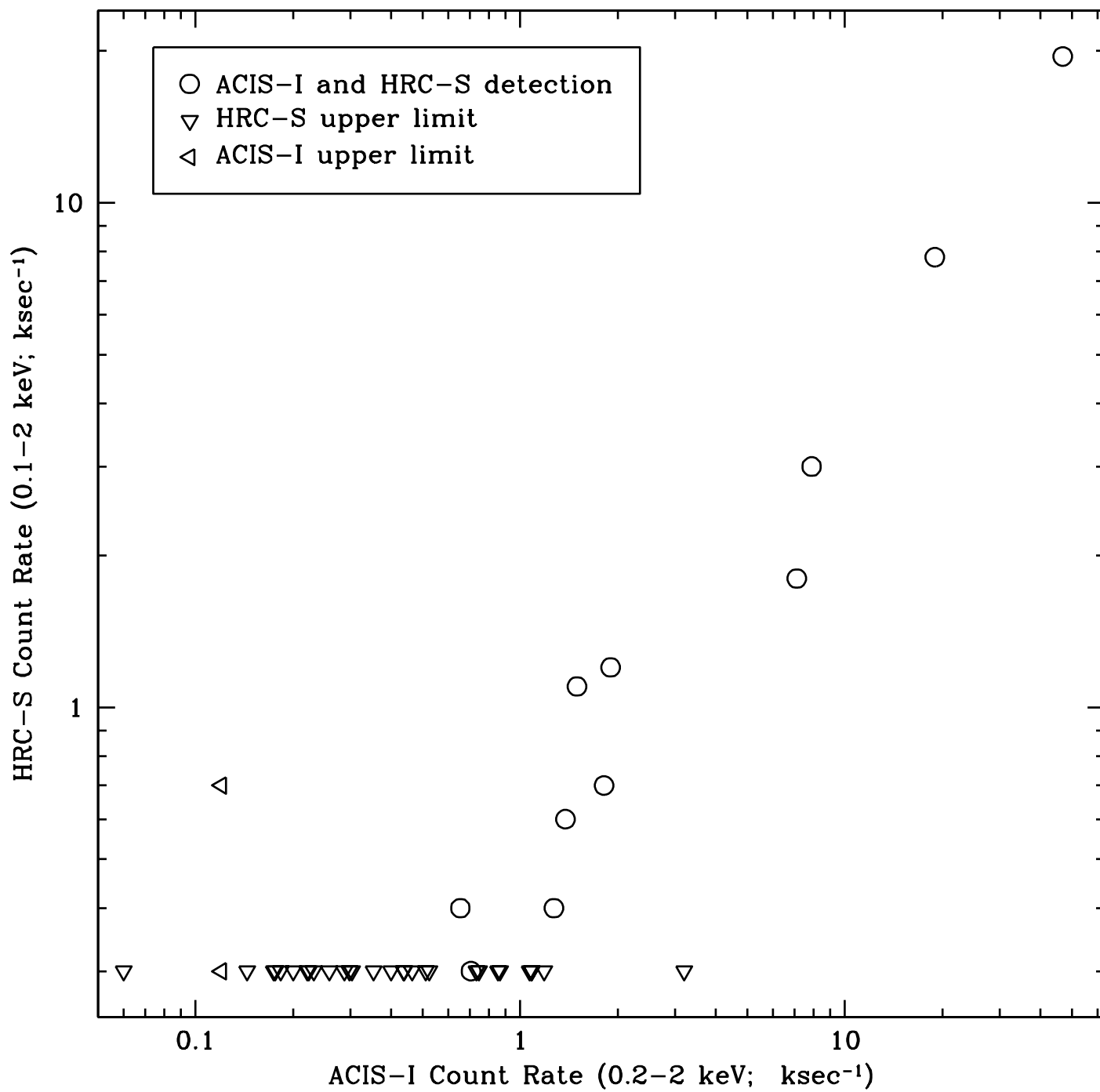


Figure 3a

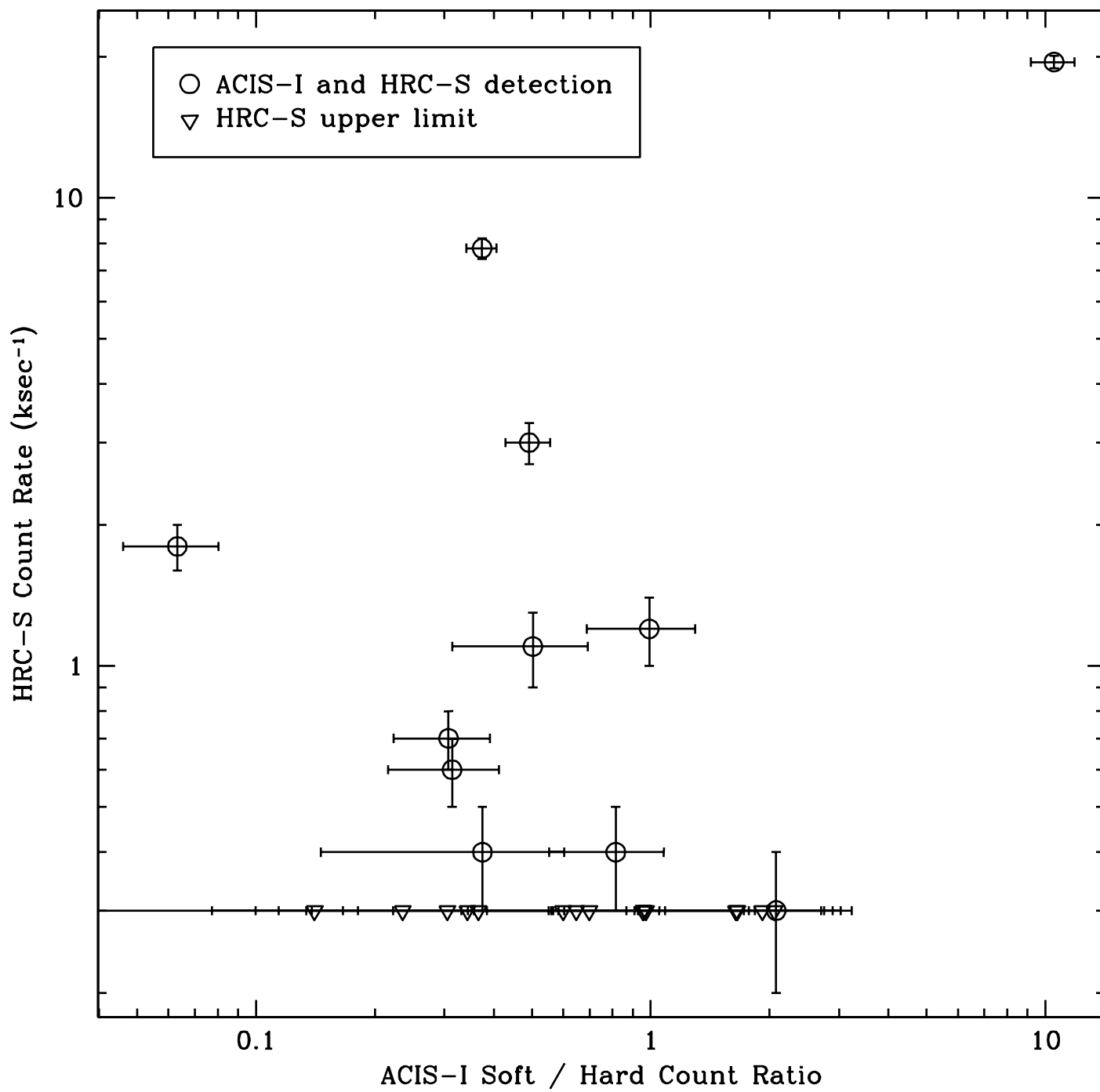


Figure 3b

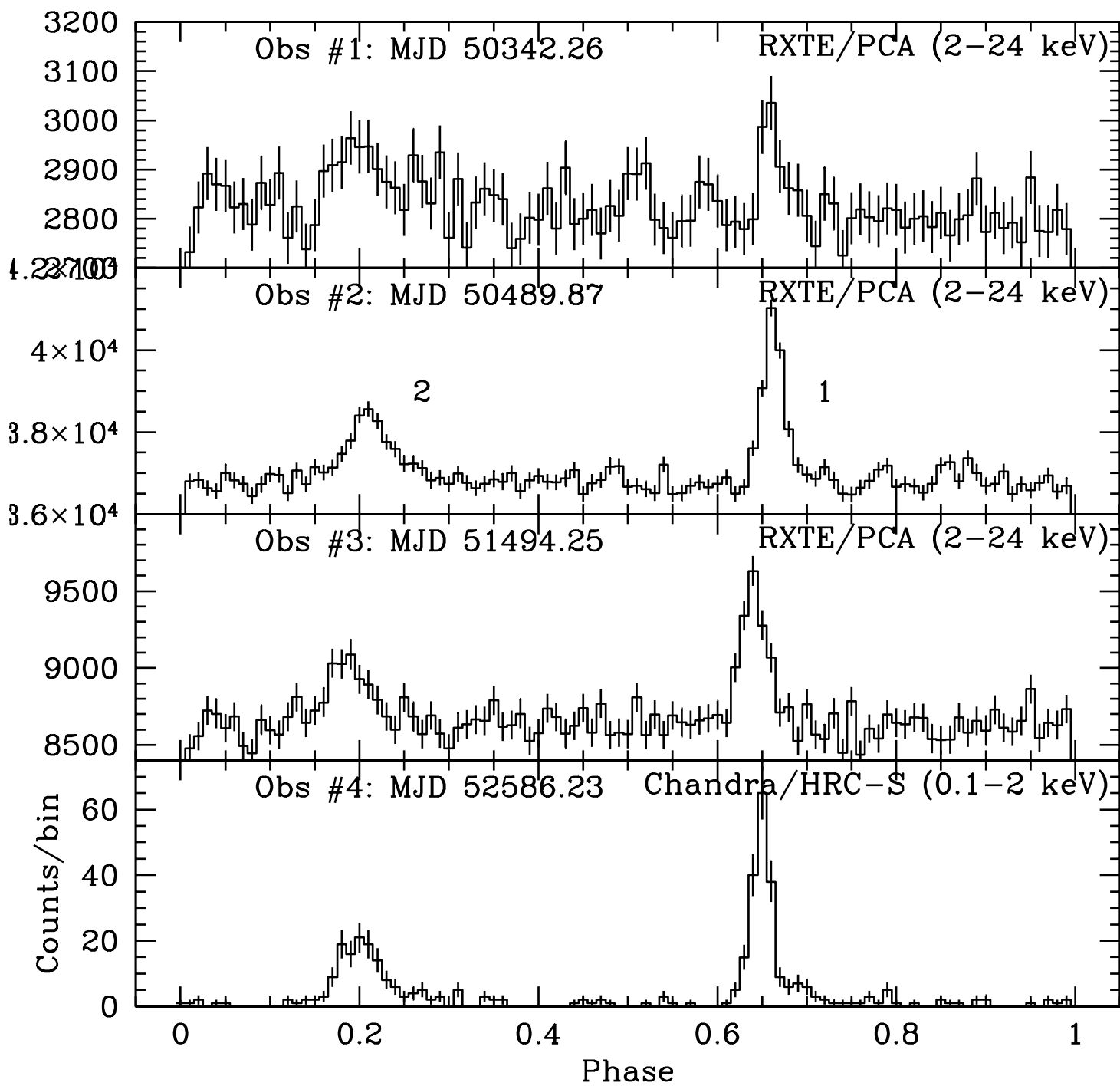


Figure 4

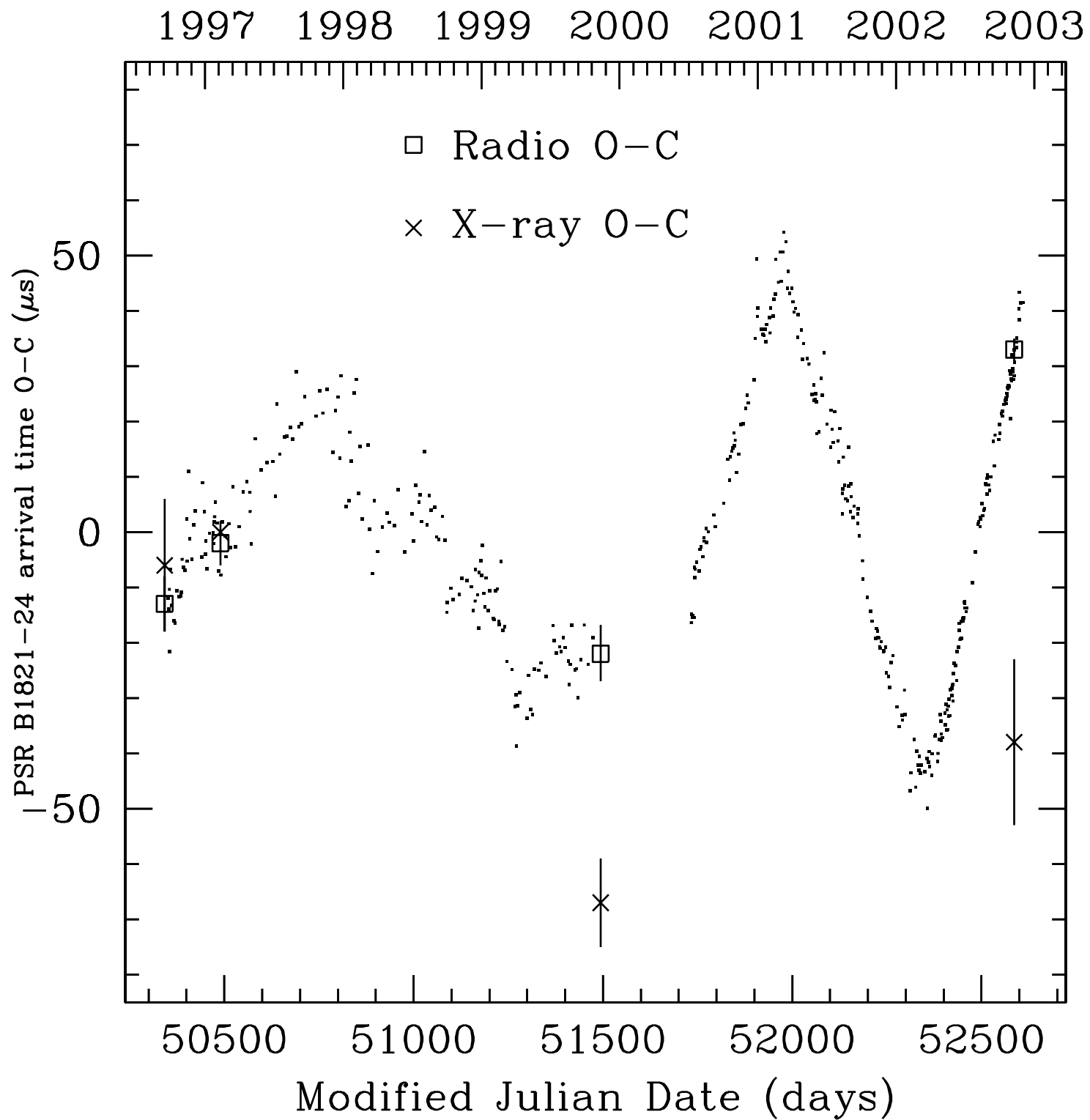


Figure 5

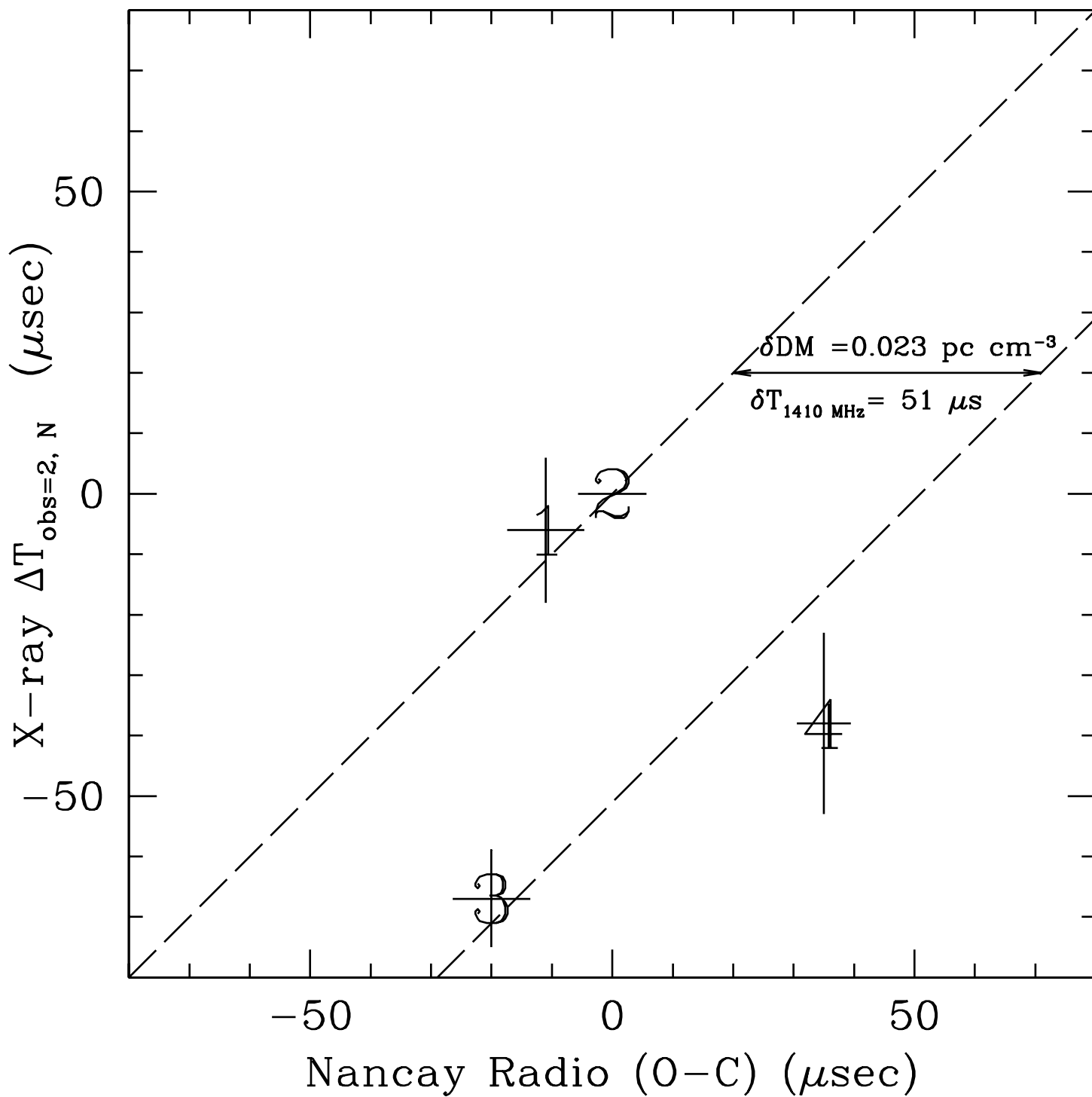


Figure 6

Table 1. Nançay Radio Ephemeris of PSR B1821–24

Parameter	Value
MJD Range	50351-52610
t_0 (MJD)	51468.0
R.A. (J2000)	18h24m32.s008345
DEC. (J2000)	−24d52m10.s758586
DM (pc cm ^{−3})	119.873
$\phi(t_0)$	−0.008(4)
ν (s ^{−1})	327.40564101150(1)
$\dot{\nu}$ (10 ^{−12} s ^{−2})	−0.1735080(1)
$\ddot{\nu}$ (10 ^{−24} s ^{−3})	0.66(1)
RMS ^a (milliperiods)	8.1
Time System	DE405

Note. — The ephemeris is not corrected for the TOA variations due to a time-variable DM, the effect of which is significant (that is, comparable or greater than the RMS variation observed). $\phi = 0$ corresponds to the average arrival phase of RP2 over the ephemeris MJD range. ^a root-mean-square deviations of Time of Arrival vs. ephemeris prediction, in milli-periods.

Table 2. Table of Observations

Obs. #	Instrument (ObsID)	Obs. Start (TT)	Obs. Start O (MJD)	Live Time) (ksec)
1	RXTE/PCA (P10421)	1996 Sep 16 06:16	50342.26	6.6
2	RXTE/PCA (P20159)	1997 Feb 10 20:57	50489.87	98.6
3	RXTE/PCA (P40090)	1999 Nov 12 11:44	51494.25	39.7
4	<i>Chandra</i> /HRC-S (2797)	2002 Nov 8 05:41	52586.23	49.1

Table 3. Catalog of *Chandra* HRC-S X-ray Sources

Label	RA (J2000.0)	Dec (J2000.0)	\pm ($''$)	Dist. to core ($'$)	HRC-S c ksec $^{-1}$ (\pm)	# from B02	
(PSR B1821–24)	9	18 24 22.590	-24 52 6.35	0.08	0.097	0.3 (0.1)	3
	8	18 24 22.682	-24 51 3.03	0.06	1.157	1.8 (0.2)	4
	12	18 24 30.428	-24 51 23.82	0.08	0.803	0.3 (0.1)	n/a
	2	18 24 31.056	-24 52 45.28	0.04	0.555	3.0 (0.3)	17
	1	18 24 32.008	-24 52 10.76	0.02	0.021	7.8 (0.4)	19
	7	18 24 32.341	-24 52 8.31	0.06	0.061	1.1 (0.2)	22
	6	18 24 32.502	-24 52 7.41	0.05	0.076	0.6 (0.1)	23
	5	18 24 32.695	-24 52 23.35	0.06	0.189	0.7 (0.1)	25
	0	18 24 32.822	-24 52 8.24	0.01	0.063	19.5 (0.6)	26
	4	18 24 33.063	-24 52 10.34	0.04	0.028	1.2 (0.2)	29
	3	18 24 33.283	-24 52 9.07	0.05	0.049	0.7 (0.1)	n/a
	11	18 24 35.506	-24 52 18.25	0.08	0.105	0.4 (0.1)	37
10	18 24 36.591	-24 50 15.71	0.09	1.939	0.4 (0.1)	38	

Note. — M28 Cluster center from Harris (1996). Astometry was performed relative to the Nançay ephemeris position (Table 1)

Table 4. Sources and Magnitude of Absolute X-ray Timing Uncertainty

Source	Magnitude
<i>Chandra</i> HRC event digitization	$\pm 5 \mu s$
<i>Chandra</i> 281 μs CCDM delay time	$\pm 10 \mu s$
<i>Chandra</i> Clock Stability	$\pm 5 \mu s$
RXTE/PCA event-UT tie (after MJD 50567)	$\pm 5 \mu s$
RXTE/PCA event-UT tie (before MJD 50567)	$\pm 8 \mu s$

Table 5. X-ray Pulse Gaussian Model

Parameter	Value
ϕ_1 (phase)	0.6621
σ_1 (phase)	0.0115
A_1	1.00 ± 0.08
ϕ_2 (phase)	0.2107
σ_2 (phase)	0.024
A_2	0.67 ± 0.07

Note. — Uncertainty in the relative normalization was found from best-fit Gaussians to the *Chandra* data.

Table 6. Observational Timing Parameters

Obs. #	Ref. Time (MJD)	ϕ (Ref. Time) (frac. phase)	ν (Ref. Time) (Hz)	$\dot{\nu}$ (Ref. Time) (10^{-12} s^{-2})
1	50342.26240326679	0.0480	327.40565789065	−0.173572
2	50489.86919495780	0.3041	327.40565567710	−0.173564
3	51494.25419383658	0.9761	327.40564061792	−0.173507
4	52586.23379831800	0.0617	327.40562425102	−0.173444

Note. — Values of ϕ (Ref. Time), ν (Ref. Time) and $\dot{\nu}$ (Ref. Time) were found using the DE405 time system ephemeris valid over MJD 50351-52610 (Table 1).

Table 7. Phases of X-ray Components XP1 and XP2, folded on Nançay Ephemeris

Obs. N	ϕ_2 (phase)	$\frac{\phi_{2,\text{obs}2} - \phi_{2,\text{obs}N}}{327.405\text{Hz}}$ (μs)	σ_2 (phase)	ϕ_1 (phase)	$\frac{\phi_{1,\text{obs}2} - \phi_{1,\text{obs}N}}{327.405\text{Hz}}$ (μs)	σ_1 (phase)	X-ray $\Delta T_{\text{obs}=2,N}$ (μs)	Radio (O−C) (μs)
1	0.199(6)	37(20)	[0.024]	0.659(3)	10(10)	[0.0115]	−6±(8,8,5)	−13±5
2	0.211(2)	(0)	0.025(3)	0.6621(6)	(0)	0.0115(5)	(0)	−2±4
3	0.186(4)	−76(14)	0.023(5)	0.640(1)	−68(4)	0.014(1)	−67±(4,5,5)	−22±5
4	0.202(3)	−27(11)	0.023(3)	0.6490(9)	−40(3)	0.0115(9)	−38±(4,12,5)	33±2

Note. — The values in square brackets were held fixed. The values in parenthesis are the uncertainty in the preceding digit(s). The uncertainties in $\Delta T_{\text{obs}=2,N}$, (μs) are: (statistical, systematic for obs. N, systematic of obs. 2).